PHYSICAL REVIEW B **84**, 014104 (2011)

Crystal defects and related stress in Y_2O_3 thin films: Origin, modeling, and consequence on the stability of the *C*-type structure

Bertrand Lacroix,[*] Fabien Paumier, and Rolly J. Gaboriaud
Institut Pprime, Département de Physique et de Mécanique des Matériaux, UPR 3346 CNRS - Université de Poitiers, SP2MI, BP 30179, 86962 Futuroscope Chasseneuil Cedex, France

(Received 25 February 2011; published 20 July 2011)

We study the impact that the crystal defects have on the *C*-type structure of rare earth sesquioxide thin films grown by ion-beam sputtering, through the example of Y_2O_3. By monitoring the energy of the argon beam used in the sputter deposition process (between 600 and 1200 eV), we show that it is possible to control the microstructure (defects concentration, stress state and phase) in the oxide layer. Two main types of defects, ascribed to the "atomic peening effect", are evidenced by high-resolution transmission electron microscopy, Rutherford backscattering spectroscopy, and nuclear reaction analysis experiments: anti-Frenkel pairs, leading to a disorder on the oxygen-vacancy network, and oxygen-vacancy dislocations loops, to accommodate the strong nonstoichiometry. From a macroscopic measurement of the residual stresses in the as-deposited and the annealed layers, through x-ray diffraction and the $\sin^2\Psi$ method, we have modeled the related stress state using an enhanced triaxial stress model. In the as-grown films, we evidence the coexistence of a biaxial and a hydrostatic stress, due to inclusions of atomic size defects. Quantitative information of the concentration and the nature of each type of defect (size effect) have also been determined, in good agreement with experiments. Interestingly, in the most energetic growth conditions corresponding to the highest degree of disorder on the oxygen-vacancy network and to the highest stress field in the film, we demonstrate that it is possible to stabilize an unexpected and metastable non equilibrium fluorite-like phase (X-type).

DOI: 10.1103/PhysRevB.84.014104 PACS number(s): 61.72.Hh, 64.60.My, 81.15.Cd, 81.05.Je

I. INTRODUCTION

Rare-earth (RE) oxides are complex materials which possess a wide range of physical and chemical properties, providing a large field of technological applications. Extensive research has been conducted in recent years on this oxide group.[1] Let us briefly recall that 15 RE elements belong to the lanthanide family, from lanthanum ($Z = 57$) to lutetium ($Z = 71$). Yttrium and scandium are added to this group because of the similarity of their outer electronic structures. The main difference between all the RE elements comes from the deep $4f$ electronic structure. In RE sesquioxides, cations are in a trivalent state, which leads to the general formula RE_2O_3.

In this work, RE_2O_3 materials are studied through the example of the yttrium sesquioxide, Y_2O_3, which exhibits a stable crystallographic phase (cubic-*C* type) up to 2325 °C (melting point at 2450 °C). This oxide is particularly interesting because of several relevant physical properties such as a high mechanical strength, a high thermal conductivity, a wide bandgap ($E_g \approx 5.5$ eV), a rather high refractive index ($n = 1.9$), and a relatively high dielectric constant ($k \approx 12$–18).[2–6] Yttrium oxide is also a well-known host material for RE atoms (europium, terbium, or thulium), which give rise to very interesting photoluminescence properties for optical applications.[7,8] In early 2000, yttria and more generally RE_2O_3 oxides thin films have been particularly investigated as high-*k* materials in order to be integrated as an oxide gate to replace SiO_2 in complementary metal-oxide semiconductor (CMOS) transistor technology.[9–12]

The unit cell of the Y_2O_3 cubic-*C* structure (Mn_2O_3 bixbyite type, space group $Ia\bar{3}$) is composed of 80 atoms, with a bulk lattice constant $a = 1.0604$ nm. The oxygen atoms are located on the (48e) sites, and yttrium atoms are located on two non equivalent cation site,[3] Y1 (8b) and Y2 (24d) [Fig. 1(a)]. All cations are sixfold coordinated: the Y1 atoms are surrounded by six neighboring oxygens at the same distance (0.230 nm), whereas the Y2 atoms have three pairs of neighboring oxygens at three different distances (0.225, 0.228, and 0.236 nm).[13] This leads to a specific arrangement of "constitutional" oxygen vacancies network [in (16c) position], respectively, along the body diagonal and face diagonal of the cubic cell [Fig. 1(b)].

In thin films, structural deviations from the "bulk" material can arise, not only because of their specific geometry (they are grown and constrained on a "thick" substrate), but also due to their growth conditions. In particular, low-energy irradiation can occur during ion-beam-growth processes (this effect is also called "atomic peening"[14]), leading to the introduction of defects in the deposited layer. The presence of defects generally changes the properties of the materials. In bulk Y_2O_3, those defects can modify its electronic structure. More precisely, Jollet *et al.*[15] pointed out that a modification of the stoichiometry, essentially due to oxygen vacancies, increases the covalent character of the oxygen-yttrium bonding. More recently, Zheng *et al.*[16] investigated, by first-principles calculations, the role of native point defects on the electronic properties in bulk yttria. Structural defects may also lead to strain and internal stresses that can affect the physical properties of the material. For example, Lim *et al.*[17] have shown that the development of preferred orientation in a TiN thin film is the consequence of both surface and strain energy minimization. In InGaN/GaN quantum-well heterostructures, strain-induced polarization can lead to the quantum confined Stark effect, which degrades the optical properties (decrease of the recombination efficiency, red-shifted emission).[18] A strong correlation between the presence of stress and the dielectric

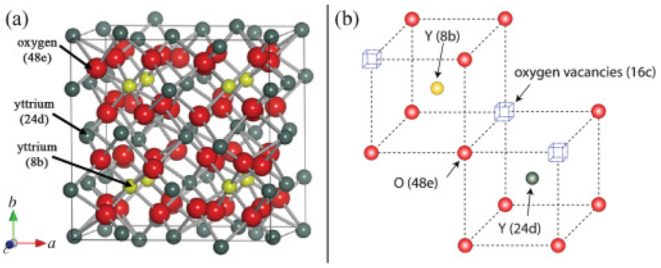

FIG. 1. (Color online) The Y_2O_3 cubic *C*-type structure (bixbyite type). (a) Unit cell representation. (b) Environment of the two Y sites (the actual position of the O atoms is slightly shifted from the corners of the cubes).

properties has been reported by Menon *et al.*[19] in ZnO thin films deposited by magnetron sputtering. Kaul *et al.*[20] also pointed out an interesting role of stress in the stabilization of thin epitaxial $RENiO_3$ films (with RE = Pr, Nd, Sm, Gd), which are unstable as bulk phases under the deposition conditions. In the literature, only a few groups of authors have already reported works devoted to the understanding of stress generated during ion-beam-deposition processes in Y_2O_3 thin films [21] (and even more generally in RE oxide thin films). Unfortunately, many questions about the physical origin, the nature, and the consequence of this stress/strain state in such oxides films remain unsolved. Can it be related to crystal defects (point or complex defects)? If yes, should it be described by a pure biaxial component or by an hydrostatic component such as in GaN?[22] Does it enable the stabilization of non equilibrium phases, which could be newer interests in the areas of ion-beam-induced patterning? To answer these questions, a detailed structural investigation of yttrium oxide thin films grown by means of the ion-beam-sputtering (IBS) technique is addressed. This paper first focuses on the identification of crystal defects which are created using this specific growth method (Sec. III). The strain and the deviations from the "ideal" structure will be then considered. An analysis of the results and the modeling of the stress state is performed in Sec. IV. Then, the thermodynamical stability of the cubic-*C* phase versus a disordered fluorite-like structure, in the presence of stress, will be discussed (Sec. V).

II. EXPERIMENTS

Yttrium oxide, Y_2O_3, thin films were deposited on (100) silicon (Si), (100) strontium titanate ($SrTiO_3$), and (100) magnesium oxide (MgO) substrates using the IBS deposition technique, in a Nordiko sputtering chamber which includes two radio-frequency (RF) sources. The primary source delivers an argon ion-beam with constant energies in a range of 600 to 1200 eV. It was used to sputter a 15-cm-diameter water-cooled Y_2O_3 sintered target, inclined by an angle of 45°. The ion-beam current was kept at 80 mA. The secondary source was used to introduce oxygen into the chamber with a flow of 5 sccm (RF is off). During the deposition process, the substrate temperature was maintained at 700 °C and the background pressure increased to 1.3×10^{-2} Pa. The deposition time was calculated in order to obtain a thickness of 100 nm for each sample. Postdeposition annealing treatments between 300 and 1000 °C were also performed in a quartz tube furnace, under air atmosphere.

The crystallographic structure of yttrium oxide thin films was investigated by combining x-ray diffraction (XRD) and high resolution transmission electron microscopy (HRTEM) experiments. XRD analyses were performed using a four-circle Siefert diffractometer equipped with copper x-ray source radiations ($\lambda_{K\alpha_1} = 0.15405$ nm, $\lambda_{K\alpha_2} = 0.15443$ nm) operating at 40 kV and 40 mA, in the Bragg–Brentano geometry. The internal stresses in the Y_2O_3 layers were determined using the $\sin^2 \Psi$ method.[23] By measuring the lattice parameter a in several crystallographic directions (denoted by Ψ), it is possible to plot the strain versus $\sin^2 \Psi$. Then, assuming a linear dependence and knowing the elastic constants of the material, the stress can be obtained from the slope of the $a = f(\sin^2 \Psi)$ straight line.

HRTEM images were acquired through a JEOL 3010 high-resolution electron microscope operating at 300 kV (LaB_6, Cs = 1.2 mm, 0.19-nm point resolution). Cross-sectional samples were beforehand thinned by mechanical polishing using a tripod polisher in order to reach a thickness lower than 10 μm. Ion milling using 2.5-keV Ar ions in grazing incidence (±5°) was then performed until obtaining an electron transparency area.

The chemical composition and stoichiometry of the Y_2O_3 films were determined by combining Rutherford backscattering spectroscopy (RBS) using a 1.7-MeV $^4He^+$ ion-beam and nuclear reaction analysis (NRA) techniques. RBS spectra were fitted using the RUMP[24] and SIMNRA[25] simulation codes.

III. STRUCTURE OF Y_2O_3 THIN FILMS

A. Growth on silicon substrate

This first part of the results is focused on the microstructural modifications of Y_2O_3 thin films as a function of the energy of the ion-beam which sputters the Y_2O_3 target. Four samples, deposited on a silicon substrate using Ar ions at 1200 eV [sample (1)], 1000 eV [sample (2)], 800 eV [sample (3)], and 600 eV [sample (4)], have been studied. Postdeposition thermal annealings of sample (1) under air atmosphere were also achieved at 300 °C during 18 h [sample (5)], at 700 °C during 4 h [sample (6)], at 900 °C during 2 h [sample (7)], and at 1000 °C during 1 h [sample (8)]. These different conditions are summarized in Table I.

The determination of the crystal orientations from the XRD θ-2θ scans indicates that all these thin films are strongly textured along the [111] direction of the cubic-*C* structure of Y_2O_3. Only one diffraction peak corresponding to the (222) planes is observed (Fig. 2). However, depending on the primary ion-beam energy used in the sputtering process, the XRD profiles are very different. For sample (4), deposited with the lower energy (600 eV), the (222) Bragg peak is almost symmetric with a position $2\theta = 28.67°$, which is slightly shifted toward the low angle values with respect to the value $2\theta_{bulk} = 29.15°$ of the bulk material. The profile of the Bragg peak is strongly modified when the primary ion-beam energy increases from 600 to 1200 eV: a strong shift toward the low angle values ($2\theta = 28.04°$), an asymmetrical profile, and a decrease of the diffracted intensity are observed. However,

TABLE I. Summary of the different Y_2O_3 thin films grown on Si, $SrTiO_3$, and MgO. The energy of the Ar beam which sputters the Y_2O_3 target and the eventual postdeposition annealing conditions (temperatures, duration) are indicated.

Sample label	Energy of the Ar beam (eV)	Substrate	Postdeposition annealing (air)
(1)	1200	Si	No
(2)	1000	Si	No
(3)	800	Si	No
(4)	600	Si	No
(5)	1200	Si	300 °C–18 h
(6)	1200	Si	700 °C–4 h
(7)	1200	Si	900 °C–2 h
(8)	1200	Si	1000 °C–1 h
(9)	1200	$SrTiO_3$	No
(10)	1200	$SrTiO_3$	700 °C–4 h
(11)	1200	MgO	No

the rocking curves obtained by scans around the (222) peak (not shown here) do not change significantly and thus cannot explain the diffracted intensity loss which is observed. After thermal annealing of sample (1) at 300 °C and 700 °C, a Bragg peak with a 2θ position close to the bulk value and a symmetric profile is recovered.

The atomic concentrations of each atomic species in as-deposited thin films (1), (2), (3), and (4), together with annealed sample (6), have been determined by RBS (see RBS spectra in Fig. 3). All the samples exhibit the same concentration of entrapped argon (due to Ar backscattered ions on the target during deposition) which is close to 2.0 at. %. A similar strong oxygen understoichiometry $Y_2O_{2.7}$ for these samples is also found, within the uncertainties of the measurements (O/Y ratio close to 1.35). The NRA measurements, which are very sensitive to light atoms, confirm that the oxygen content in each as-deposited sample is identical. After annealing of sample (1) at 700 °C, a slight increase of the oxygen content, from 427.10^{15} at./cm^2 to 440.10^{15} at./cm^2, is observed: This corresponds to an increase of only 3%, within the accuracy range of the technique. The annealing of sample (1) at 1000 °C leads to a strong modification of the stoichiometry, with a significant increase of the oxygen amount up to 720.10^{15} at./cm^2: obviously, such an increase of more than 60% takes into account not only an increase (not quantitative) of the stoichiometry in the yttria film due to introduction of oxygen from air, but also a silicate formation at the inteface as observed before.[26]

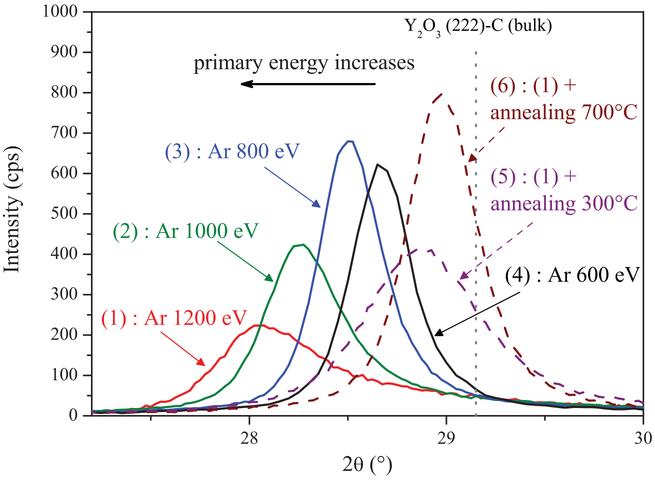

FIG. 2. (Color online) Evolution of the (222) Bragg peak (θ-2θ), along the growth direction, of the as-deposited thin films on Si as a function of the Ar beam energy used in the sputtering process: sample (1), 1200 eV; sample (2), 1000 eV; sample (3), 800 eV; sample (4), 600 eV; and after thermal annealing of sample (1) at 300 °C and 700 °C.

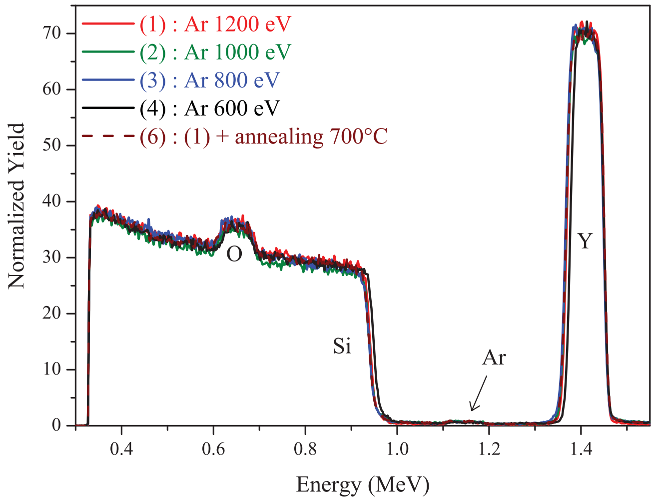

FIG. 3. (Color online) Random RBS spectra of the as-deposited samples [(1), (2), (3), (4)] and the sample annealed at 700 °C (6) (growth on Si substrate).

B. Growth on $SrTiO_3$ and MgO substrates

To get other microstructural insights of Y_2O_3 thin films deposited by IBS, complementary studies were performed using different substrates. First, with $SrTiO_3$ substrates, it has been shown previously[27] that Y_2O_3 grows along the [100] direction, with an in-plane epitaxial relationship following the $[001]_{Y_2O_3}$ axis parallel to the $[110]_{SrTiO_3}$ axis. Furthermore, on MgO substrates, Y_2O_3 grows epitaxially with four variants along the [111] axis.[28] These epitaxial relationships are particularly relevant for HRTEM investigations in cross-section.

In this part, three samples are considered (see the summary in Table I): on $SrTiO_3$, the as-deposited thin film using argon ions at 1200 eV [sample (9)] and the annealed sample at 700 °C during 4 h under air atmosphere [sample (10)]; on MgO, the as-deposited thin film, using argon ions at 1200 eV [sample (11)].

As shown in Fig. 4, the (222) and (400) Bragg peaks along the growth direction (corresponding respectively to Y_2O_3 deposited on Si, MgO, and $SrTiO_3$, with a 1200-eV Ar ion-beam) exhibit the same features (asymmetric profile, strong shift toward the low angles) whatever the substrate is. Moreover, all the samples have the same behavior after thermal annealing (not shown here), with an XRD peak which becomes symmetric and close to the bulk value. Consequently all these considerations indicate that these features are intrinsically due to the deposition technique: therefore, thin films grown

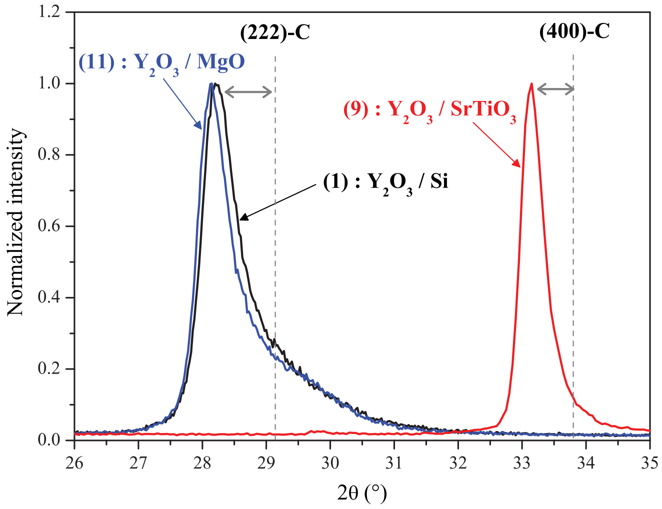

FIG. 4. (Color online) Y_2O_3 Bragg peaks corresponding to the (222) reflection with Si and MgO substrates and to the (400) with $SrTiO_3$ substrate (as-deposited films using the Ar 1200-eV sputtering beam).

on MgO and $SrTiO_3$ can be used as model samples for investigation by means of HRTEM.

The HRTEM cross-section image of sample (9) seen along the [001] zone axis of Y_2O_3, in the vicinity of the interface $Y_2O_3/SrTiO_3$ (Fig. 5), exhibits two different contrasts. The local fast Fourier transforms (FFTs) (square region of 17 x 17 nm^2), obtained through the Digital Micrograph software (Gatan), change significantly depending on the region where the analysis is performed. In FFT(a), the typical order spots related to the oxygen ordered network in the cubic-*C* structure are visible. In FFT(b), these order spots become very faint and tend to disappear. After an annealing at 700 °C [sample (10)], only one contrast is evidenced, and clearly shows the presence of the order spots on the FFT pattern (Fig. 6). These features will be explained in the next part (Sec. III C).

Along the $[01\bar{1}]$ zone axis of Y_2O_3 grown on $SrTiO_3$, another particular contrast which exhibits a lamellar shape is observed. This contrast is systematically inclined by 54.7° from the surface and it is interpreted in terms of planar defects in the $\{111\}$ planes (Fig. 7).

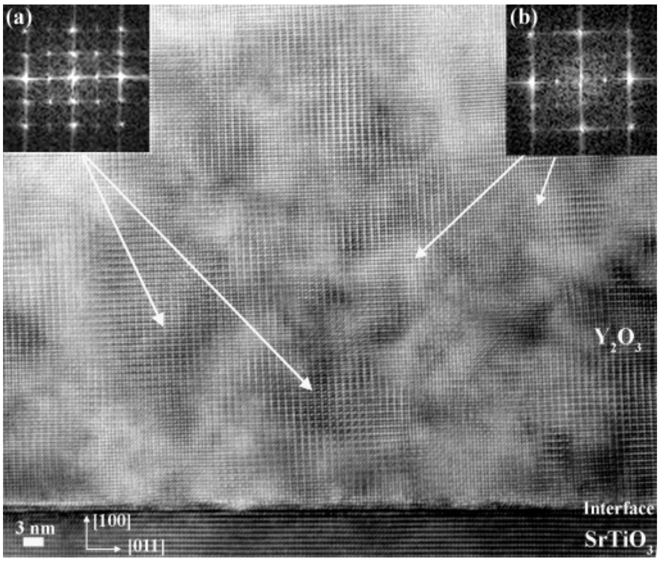

FIG. 5. HRTEM cross-section image of $Y_2O_3/SrTiO_3$ interface [sample (9)], seen along the [001] zone axis. The insets correspond to the local FFT performed on different areas indicated by white arrows. FFT(a): order spots are clearly evidenced (cubic-*C*). FFT(b): order spots are not present or very faint (disordered cubic-*C*).

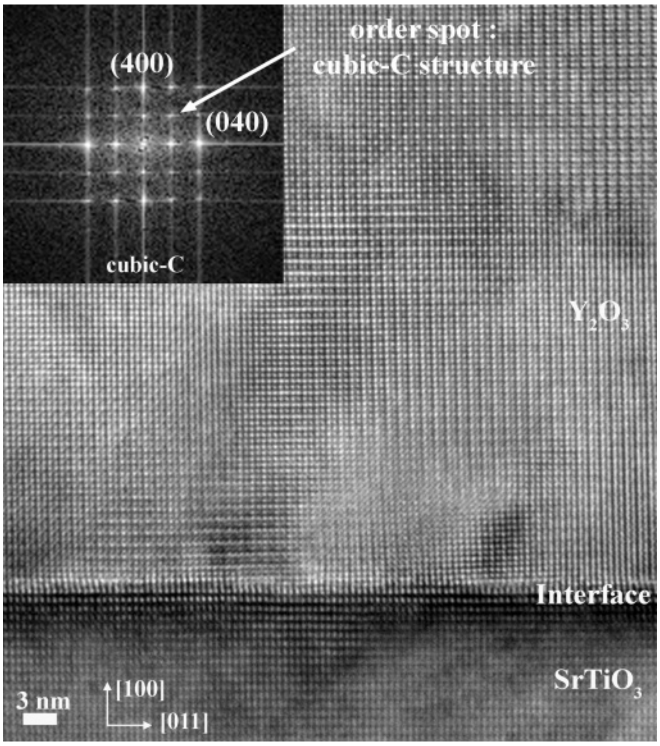

FIG. 6. HRTEM cross-section image of $Y_2O_3/SrTiO_3$ interface after an annealing at 700 °C [sample (10)], along the [001] zone axis. Typical order spots of the cubic-*C* structure are systematically observed on the FFT pattern.

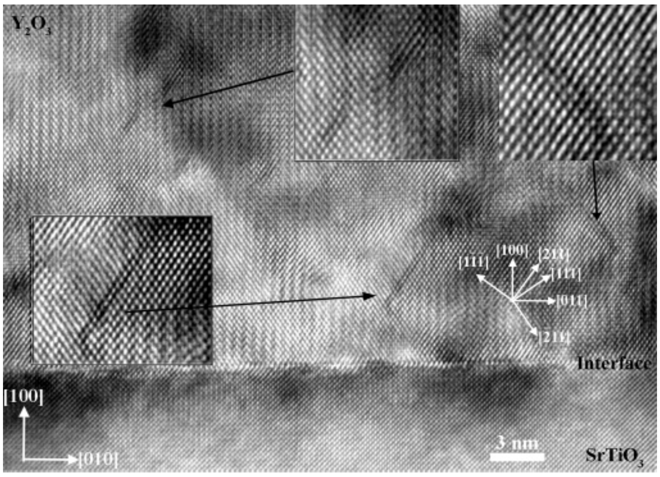

FIG. 7. HRTEM cross-section image of $Y_2O_3/SrTiO_3$ interface [sample (9)] along the $[01\bar{1}]$ zone axis: Lamellar defects are evidenced and ascribed to planar defects in the $\{111\}$ planes and shown in the insets.

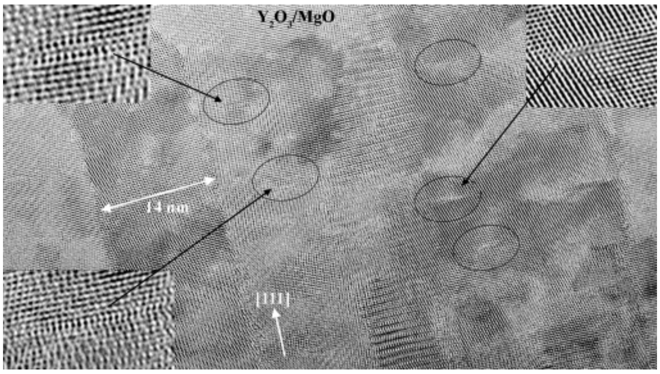

FIG. 8. HRTEM cross-section image of Y_2O_3/MgO interface [sample (11)]: Lamellar defects are evidenced and ascribed to planar defects in the $\{111\}$ planes and shown in the insets.

The same HRTEM observations have been performed on sample (11) (Y_2O_3/MgO). The cross-section image of the film (Fig. 8) also show a high density of lamellar defects, also ascribed to planar defects in the $\{111\}$ planes. The columnar character of the layer, where the crystallites have a lateral dimension of around 14 nm, can also be noticed.

C. Discussion: Results on the microstructure

The RBS/NRA measurements highlight two interesting features in the Y_2O_3 thin films grown by IBS. First, a significant amount of backscattered Ar ions is entrapped with a concentration of 2 at. % after deposition, whatever the energy of the Ar beam involved in the target sputtering process. This argon concentration remains unchanged after the different thermal annealing treatments. Moreover, the yttria thin films are not stoichiometric. This nonstoichiometry ($Y_2O_{2.7}$) is ascribed to an excess of oxygen vacancies in comparison with the 25% of constitutional oxygen vacancies in the (16c) position. The atomic configuration of this excess of oxygen vacancies cannot be clearly experimentally identified [neutral or charged oxygen atoms missing in the (48e) position,[16] bivacancies, *n*-vacancies complex or others]. It is worth noting that the stoichiometry is almost the same in the samples before and after annealing at 700 °C in air (3% increase). This result points out a relatively high stability of the atomic vacancy arrangement. In fact, NRA experiments evidenced a slight increase of the oxygen content after annealing at 700 °C, which becomes considerable after annealing at 1000 °C. Thus, in the following, we will consider that the annealing performed in the range of 300–1000 °C introduce oxygen, and modify the stoichiometry of the films.

Such understoichiometry $YO_{1.35}$ for the cubic-*C* phase is not consistent with the study of Solov'eva[29] that evidenced a very narrow margin between oxygen concentration and the different phases in yttria ($YO_{1.495}$ and $YO_{1.35}$ for the monoclinic and hexagonal structures, respectively). Therefore it seems that the stoichiometry accommodation mechanism in IBS-deposited yttria thin films, far from thermodynamic conditions, could be drastically different. One possible explanation between the stoichiometry accommodation and the observed extended defects (lamellar shape) will be discussed in detail in Sec. V. Whatever the arrangement of the oxygen-vacancy excess is, it is supposed not to modify the ordered network of constitutional oxygen vacancies, which is specific to the cubic-*C* structure [(16c) position].

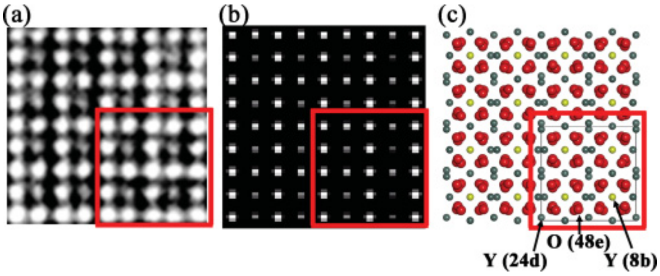

FIG. 9. (Color online) Image contrast of the Y_2O_3 *C*-type structure seen along [001]: (a) HRTEM image, (b) simulated image, (c) unit cell representation (only yttrium atoms are visible in the experimental and simulated HRTEM images).

The HRTEM investigations which have been performed on thin films deposited on $SrTiO_3$ after annealing exhibit only one type of contrast along the [001] zone axis (Fig. 6): It is in good agreement with image simulations, using the JEMS software,[30] of the *C*-type structure seen along the [001] zone axis (see Fig. 9). The different intensities of the white spots in Fig. 9(a) and Fig. 9(b) comes from the two different yttrium sites and are the signature of the constitutional oxygen-vacancy network [in the (16c) position] in the cubic-*C* phase [see Fig. 9(c)]. The lack of order spots in the FFT pattern of the as-deposited film can be assigned to anti-Frenkel pair formation (labeled AF in this paper). It is one of the native point defect pairs which has the lowest formation energy in Y_2O_3:[16] an oxygen atom which moves from a (48e) position toward one constitutional vacancy (16c) position becomes an oxygen interstitial, leaving one oxygen-vacancy in the (48e) position. This disordering mechanism due to AF pair formation is attributed to the energetic backscattered particles involved during IBS deposition which hit the surface of the sample as the growth proceeded. The corresponding areas on TEM images could be therefore attributed to a local disordering of the anionic network in the *C*-type phase which could be considered as a fluorite-like structure ($Fm\bar{3}m$ space group) when the oxygen network is highly disordered.

The HRTEM experiments of the as-deposited thin films grown on $SrTiO_3$ and MgO substrates also evidence another contrast which is ascribed to planar defects formed into the $\{111\}$ planes (Figs. 7 and 8). Such a contrast could be due to a local accommodation mechanism of the oxygen nonstoichiometry. Owing to the crystallographic model proposed by Hyde,[31] accumulation of oxygen vacancies in the $\{111\}$ planes can lead to a collapse of the lattice along the $\langle 111\rangle$ direction, followed by a crystallographic shear along the $\langle 211\rangle$ axes. The result is the formation of vacancy dislocation loops in the $\{111\}$ planes. This new stacking sequence [Fig. 10(a)] also corresponds to a nucleus of the monoclinic phase of yttria, as observed by HRTEM [Fig. 10(b)].

IV. STRAIN AND INTERNAL STRESS

The internal stress state of the films described above has been investigated by mean of the $\sin^2\Psi$ method. The $a^{hkl}_{\Phi,\Psi}$ lattice parameter in several (Φ,Ψ) directions is measured in

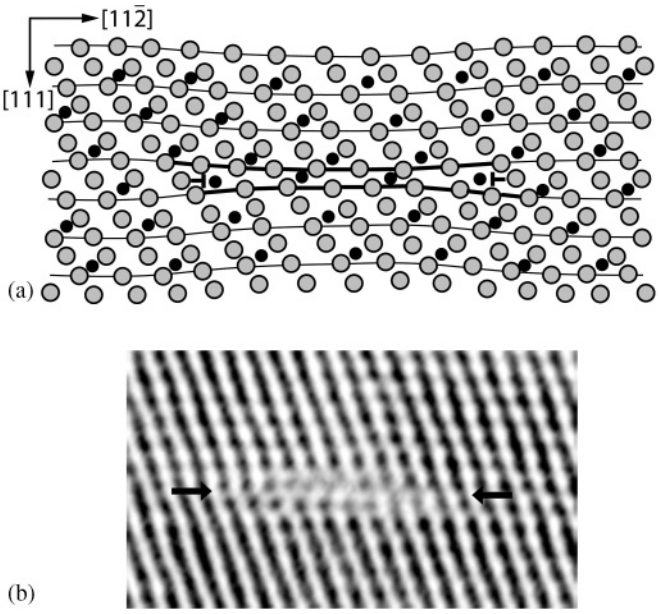

FIG. 10. Accumulation of oxygen vacancies in the {111} planes of the cubic-*C* (bixbyite) structure: (a) Schematic representation of a dislocation loop formation from Ref. 31 (gray circle, oxygen atoms; black circles, yttrium atoms). (b) HRTEM image interpreted as a dislocation loop in the (111) plane of Y_2O_3 deposited on MgO.

the laboratory coordinate system {L}, from XRD profiles of an (hkl) plane family, and the strained lattice parameter is plotted versus $\sin^2\Psi$. Φ and Ψ are respectively the rotation angle around the normal of the (hkl) planes and the tilt angle between the normal of the specimen surface and the normal of (hkl) planes (see Fig. 11). The lattice strain in the sample coordinate system {S} (taking S_3 normal to the surface of the film), along the (Φ,Ψ) direction, can be written as

$$\epsilon_{\Phi,\Psi}^{hkl} = \frac{a_{\Phi,\Psi}^{hkl} - a_{\mathrm{ref}}}{a_{\mathrm{ref}}}, \quad (1)$$

where a_{ref} is the "stress-free" lattice parameter. By combining Eq. (1) with the elasticity theory, the stress in the structure can be determined: Hooke's law gives the relationship $\epsilon_i = s_{ij}\sigma_j$ between the elements of the strain tensor ϵ_i and the stress tensor σ_j using the four-rank stiffness tensor, whose elements s_{ij} are expressed in the {S} axis system with Voigt's notations.

In polycrystalline thin films, a particular (hkl) reflection is generally investigated at different specimen tilt angles corresponding to the angle between the surface of the specimen and the (hkl) plane. In thin films grown by physical vapor deposition, preferential orientations are generally observed. Depending on the substrate and the deposition conditions, fiber-like texture growth (the crystallites are randomly oriented in-plane) or single-crystal growth (with epitaxial relationship) may occur. As a consequence, it means that the strain can be measured only in specific directions, so that the classical $\sin^2\Psi$ method cannot be used. Hauk *et al.*[32] developed an alternative approach, called the crystallite group method (CGM), which considers all the crystallites with the same orientation as unique crystals. Thus the stress determination will consist of measuring the lattice strains of different (hkl) planes family.

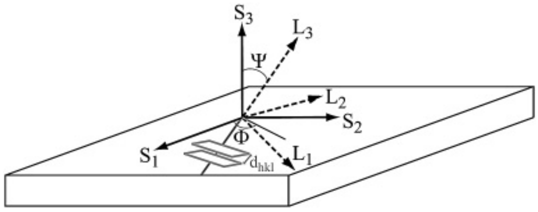

FIG. 11. Sample {S} and laboratory {L} coordinate systems.

A. Biaxial stress model

1. *Description of the biaxial model*

A cubic material elastically anisotropic, with three independent elastic compliance constants s_{11}, s_{12}, and s_{44}, is considered. From the CGM, Clemens and Bain[33] give an analysis of residual stress in thin films having a textured growth with a cubic symmetry. In this model, they assume that the particular thin film/substrate geometry allows the layer to expand freely along the growth direction (axis 3) which implies $\sigma_{13} = \sigma_{23} = \sigma_{33} = 0$. This means that the film is in a biaxial stress state. With the assumption of an equal in-plane biaxial stress ($\sigma_{11} = \sigma_{22} = \sigma_{//}$), the stress tensor can be written as

$$\bar{\bar{\sigma}} = \begin{pmatrix} \sigma_{//} & 0 & 0 \\ 0 & \sigma_{//} & 0 \\ 0 & 0 & 0 \end{pmatrix}. \quad (2)$$

The lattice parameter in any (Φ,Ψ) direction is given, for [111] growth orientation, by Eq. (3), with the anisotropy factor $J = s_{11} - s_{12} - s_{44}/2$:

$$a_{\Psi}^{111} = a_{\mathrm{ref}}\left[1 + \left(2s_{12} + \frac{2}{3}J + \frac{s_{44}}{2}\sin^2\Psi\right)\sigma_{//}\right]. \quad (3)$$

The stress analysis using Eq. (3) is valid for both fiber-textured and epitaxial thin films and can therefore be applied for this paper. The elastic constants which are used here were experimentally determined by Palko *et al.*[34] for bulk Y_2O_3.

2. *Use of the biaxial model*

Experimental $a_\Psi = f(\sin^2\Psi)$ plots, related to the as-deposited and annealed thin films deposited on Si substrate, are shown in Fig. 12. a_{ref} and $\sigma_{//}$ values obtained from the best fits using Eq. (3) increase significantly with the primary ion energy. A significant stress relaxation is observed after the annealing treatment at 300 °C (the slope of the straight lines decreases). All these values are reported in Table II.

The use of the biaxial model leads to a_{ref} values (between 10.61 and 10.84 Å) which strongly differs from the bulk value ($a_0 = 10.604$ Å). It is also worth noticing that all the lines corresponding to the as-deposited thin films and the annealed one at 300 °C intersect at $\sin^2\Psi = 1$. The same behavior is observed for Y_2O_3 deposited on MgO and $SrTiO_3$ (not shown here). Another intersection is also observed for $\sin^2\Psi = 0.7$ between the lines corresponding to the different annealed samples. These experimental $\sin^2\Psi$ intersections values are both rather far from the theoretical strain-free direction given by $\sin^2\Psi^* = \frac{2(J+3s_{12})}{3(J-s_{11}+s_{12})} = 0.44$ (for the [111] growth orientation). Moreover, it is also difficult to understand how the quasi-spherical symmetry of the strain induced by point

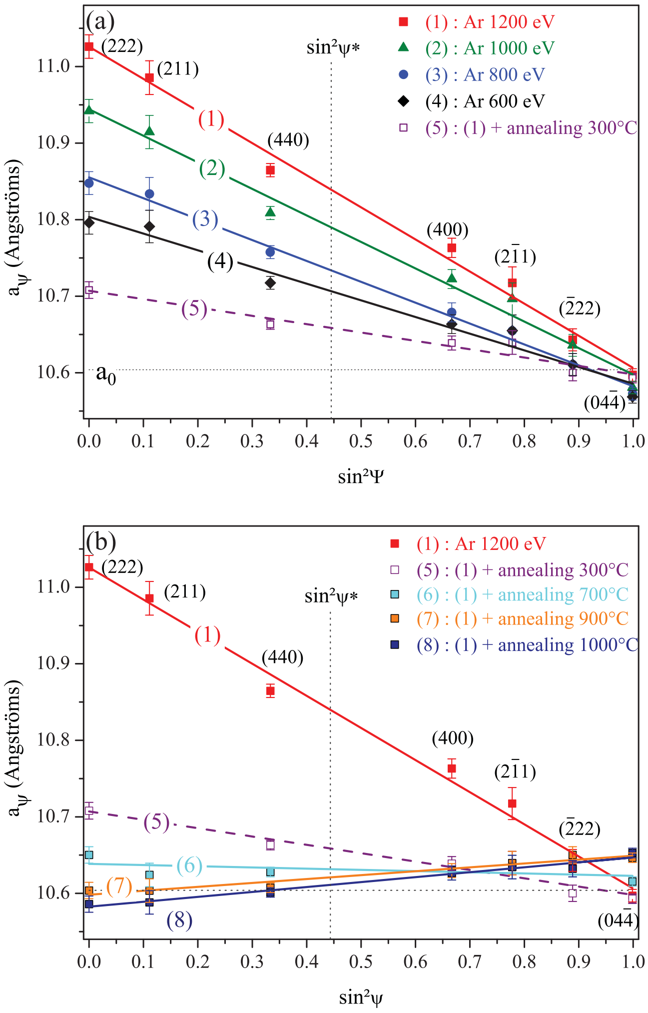

FIG. 12. (Color online) Experimental $a_\Psi = f(\sin^2\Psi)$ plots (symbols) and fits using the biaxial stress model (lines) for (a) as-deposited Y_2O_3 thin films and after annealing at 300 °C and (b) as-deposited Y_2O_3 thin films (Ar 1200 eV) and after annealing at different temperatures (on Si). The bulk lattice parameter a_0 and the strain-free direction given by $\sin^2\Psi^*$ are also depicted.

defects (AF pairs, argon, and oxygen vacancies) or extended defects with their own stress field symmetry could induce only an in-plane biaxial stress. Therefore, these considerations show that the simple description in terms of purely biaxial stress state in yttrium oxide thin films grown by IBS is not satisfying and it must be improved.

TABLE II. Stress and stress-free lattice parameter values deduced from the $\sin^2\Psi$ measurements, using the biaxial stress model (Y_2O_3/Si).

Sample	Biaxial model (Y_2O_3/Si) $\sigma_{//}$ (GPa)	a_{ref} (Å)
(1)	−5.8 ± 0.7	10.84 ± 0.01
(2)	−4.8 ± 0.7	10.79 ± 0.01
(3)	−3.8 ± 0.5	10.73 ± 0.01
(4)	−2.9 ± 0.7	10.71 ± 0.01
(5)	−1.5 ± 0.5	10.66 ± 0.01
(6)	−0.2 ± 0.5	10.63 ± 0.01
(7)	0.7± 0.3	10.62 ± 0.01
(8)	0.9± 0.3	10.61 ± 0.01

B. Triaxial stress model

1. *Description of the triaxial model*

In recent articles, an original stress model has been developed to take into account atom entrapment and defect creation during the so-called "atomic peening" in magnetron sputtered TiN films.[35–37] The stress state is described by a triaxial hydrostatic component due to the insertion of misfitting particles and a biaxial component arising from the equalization of the lateral dimensions of the film and the substrate. The body is defined as a spherical hole-containing layer with a matrix of bulk lattice parameter a_0 (E and ν are the Young's modulus and the Poisson ratio, respectively) and the stress generation in the matrix is described in two steps.

In the first step, misfitting particles (P) are randomly inserted in the holes (H) of the free-standing body, inducing a volume change $(\frac{\Delta V}{V})_F = nV_{\mathrm{mis}}$ of the film (F). The term $V_{\mathrm{mis}} = V_P - V_H$ represents the elementary volume change due to the introduction of one particle. The corresponding hydrostatic stress σ_{hyd} in the elastically isotropic matrix (M) can be calculated using Eshelby's model,[38] assuming that n spherical particles per unit volume are introduced [see Eq. (4)].

$$\sigma^M_{\mathrm{hyd}} = \frac{2}{9}\frac{E}{1-\nu}nV_{\mathrm{mis}}. \tag{4}$$

The dilated parameter of the defective body becomes $a_{\mathrm{def}} = a_0(1 + \frac{1-2\nu}{E}\sigma_{\mathrm{hyd}})$.

In the second step, the film is fixed on the substrate. A biaxial fixation stress σ_{fix} is required to fit the lateral dimensions of the dilated body on the substrate. In the work of Kamminga *et al.*,[35,36] two limiting cases of "large misfit" and "small misfit" have been considered, depending on the size effect of the particles, leading to different relationships between σ_{hyd} and σ_{fix}.

Assuming that elastic constants between the matrix and the particles are the same, we have $\sigma_{\mathrm{hyd}} = -\frac{2}{3}\sigma_{\mathrm{fix}}$ for a "large misfit" (the particle plus the surrounding matrix atoms can be considered as an entity playing the role of a macroscopic misfitting particle whose diffraction does not contribute to the diffraction peaks of the matrix), and $\sigma_{\mathrm{hyd}} = -\frac{1-\nu}{1-2\nu}\sigma_{\mathrm{fix}}$ for a "small misfit" (the displacements of the matrix atoms surrounding the inserted atom are so small that the contribution of these matrix atoms to the diffraction peaks does not disappear). This concept of small and large misfit will be discussed later in Sec. V. Equation (4) that relies σ^M_{hyd} to n and V_{mis} is valid only for the case of "large misfit" particles. For "small misfit" we have

$$\sigma^M_{\mathrm{hyd}} = \frac{E}{3(1-2\nu)}nV_{\mathrm{mis}}. \tag{5}$$

Considering that the elastic constants and the size effects of the misfitting particles are generally unknown, Abadias and Tse[37] introduced an adjustment parameter β to link the hydrostatic and the fixation components. It is defined by

$$\sigma_{\mathrm{hyd}} = -\beta\sigma_{\mathrm{fix}}. \tag{6}$$

For films having the [111] growth orientation, β can vary between $\beta_{\mathrm{min}} = \frac{2}{3}$ and $\beta_{\mathrm{max}} = \frac{s_{11}+s_{12}-J/3}{s_{11}+s_{12}}$, corresponding to the limiting cases of Refs. 35 and 36.

If the thin film deposition is performed at a temperature T_{dep}, different from the room-temperature T_{room}, and if the thermal expansion coefficients of the substrate $[\alpha_S(T)]$ and the film $[\alpha_F(T)]$ are not the same, a biaxial thermal stress σ_{th}, given by Eq. (7), needs to be added.

$$\sigma_{\mathrm{th}} = \frac{E}{1-\nu}\int_{T_{\mathrm{dep}}}^{T_{\mathrm{room}}} [\alpha_S(T) - \alpha_F(T)]\, dT. \tag{7}$$

From the linear thermal expansion found in the literature,[34,39] the calculation gives $\sigma_{\mathrm{th}} = 0.6$ GPa for Y_2O_3 deposited on Si at 700 °C. This component is significant and needs to be taken into account to describe the stress state. But, it does not fully explain our results and the strong modifications of the slopes of the $a_\Psi = f(\sin^2\Psi)$ straight lines remain unclear.

Finally, the resulting triaxial stress tensor is given by Eq. (8). It is compatible with the condition of free expansion of the film along the growth direction ($\sigma_{33} = 0$), which is generally assumed for thin layers. This implies that a stress relaxation may occur among the first atomic layers near the surface, when the deposition is achieved.

$$\bar{\bar{\sigma}} = \begin{pmatrix} \sigma_{\mathrm{hyd}}\left(1-\frac{1}{\beta}\right)+\sigma_{\mathrm{th}} & 0 & 0 \\ 0 & \sigma_{\mathrm{hyd}}\left(1-\frac{1}{\beta}\right)+\sigma_{\mathrm{th}} & 0 \\ 0 & 0 & \sigma_{\mathrm{hyd}} \end{pmatrix}. \tag{8}$$

The $a_\Psi = f(\sin^2\Psi)$ equation for the [111] growth axis deduced from Hooke's law becomes, for the general case of an anisotropic material,

$$a_\Psi^{111} = a_0[1+(s_{11}+2s_{12})\sigma_{\mathrm{hyd}}]\left[1+\left(2s_{12}+\frac{2}{3}J+\frac{s_{44}}{2}\sin^2\Psi\right)\left(\sigma_{\mathrm{th}}-\frac{\sigma_{\mathrm{hyd}}}{\beta}\right)\right]. \tag{9}$$

In Table III are reported the analytical expressions of the $\sin^2\Psi$ lines intersections from Ref. 37. In the specific situation of layers having the same growth stress (σ_{hyd}) and different thermal (biaxial) stresses (σ_{th}), the $\sin^2\Psi$ lines will intersect at a point labeled $*$. This corresponds to the biaxial stress model with $a_{\mathrm{ref}} = a_0[1+(s_{11}+2s_{12})\sigma_{\mathrm{hyd}}]$. In the other case of layers having different growth stresses and equal thermal stresses, the $\sin^2\Psi$ lines will intersect at a new point labeled c, which depends among others on β. Thus, if the intersection is clearly identified, the value of β can be easily determined.

TABLE III. Analytical expressions of the $a_\Psi = f(\sin^2\Psi)$ intersections for the [111] growth orientation (Ref. 37).

Equal σ_{hyd} and different σ_{th}	$\sin^2\Psi^* = \frac{2(J+3s_{12})}{3(J-s_{11}+s_{12})}$ $a^* = a_0[1+(s_{11}+2s_{12})\sigma_{\mathrm{hyd}}]$
Different σ_{hyd} and equal σ_{th}	$\sin^2\Psi_c = \frac{\beta s_{11}-2s_{12}(1-\beta)-2J/3}{s_{11}-s_{12}-J}$ $a_c = a_0\,[1+\beta\,(s_{11}+2s_{12})\,\sigma_{\mathrm{th}}]$

2. Improvement of the triaxial model

The previous Eq. (9) is valid for films having only one type of defect (with a specific value of β). In this paper, three types of defects, considered as particles, have been identified: the backscattered Ar ion entrapped in the layer (Ar), the oxygen vacancies related to the nonstoichiometry (vac) and the anti-Frenkel defects (AF). Equation (9) can be generalized considering the effective (total) hydrostatic (fixation, respectively) stress as the sum of the hydrostatic (fixation, respectively) stresses due to each type of defect (i):

$$\sigma^{\mathrm{eff}}_{\mathrm{hyd,fix}} = \sum_i \sigma^{(i)}_{\mathrm{hyd,fix}} = \sigma^{\mathrm{Ar}}_{\mathrm{hyd,fix}} + \sigma^{vac}_{\mathrm{hyd,fix}} + \sigma^{\mathrm{AF}}_{\mathrm{hyd,fix}}.$$

The relationship between the hydrostatic and the fixation stresses remains valid for each type of defect (i), as indicated by

$$\sigma^{(i)}_{\mathrm{hyd}} = -\beta^{(i)}\sigma^{(i)}_{\mathrm{fix}}. \tag{10}$$

The resulting $a_\Psi = f(\sin^2\Psi)$ equation is given by:

$$a_\Psi^{111} = a_0\left[1+(s_{11}+2s_{12})\sigma^{\mathrm{eff}}_{\mathrm{hyd}}\right]\left[1+\left(2s_{12}+\frac{2}{3}J+\frac{s_{44}}{2}\sin^2\Psi\right)\left(\sigma_{\mathrm{th}}+\sigma^{\mathrm{eff}}_{\mathrm{fix}}\right)\right]. \tag{11}$$

3. Use of the triaxial model

To solve this problem (determination of $\beta^{(i)}$ and $\sigma^{(i)}_{\mathrm{hyd}}$), appropriate conditions for which modifications of concentration of only one type of defect occur must be found. When only one type of defect concentration (i) changes while the others keep fixed, the analytic expression on the $a_\Psi = f(\sin^2\Psi)$ lines intersection is

$$\sin^2\Psi^{(i)}_c = \frac{\beta^{(i)}s_{11}-2s_{12}(1-\beta^{(i)})-2J/3}{s_{11}-s_{12}-J}. \tag{12}$$

The RBS results evidenced that the argon distribution remains unchanged after annealing at 700 °C and even at 1000 °C (not shown here). This implies that the contribution of the entrapped Ar on the residual stresses is very low by comparison with the AF and vac contributions, and we will suppose that $\sigma^{\mathrm{Ar}}_{\mathrm{hyd}} = 0$. Thus, Eq. (11) becomes

$$a_\Psi^{111} = a_0\left[1+(s_{11}+2s_{12})\left(\sigma^{\mathrm{AF}}_{\mathrm{hyd}}+\sigma^{vac}_{\mathrm{hyd}}\right)\right]\left[1+\left(2s_{12}+\frac{2}{3}J+\frac{s_{44}}{2}\sin^2\Psi\right)\left(\sigma_{\mathrm{th}}-\frac{\sigma^{\mathrm{AF}}_{\mathrm{hyd}}}{\beta^{\mathrm{AF}}}-\frac{\sigma^{vac}_{\mathrm{hyd}}}{\beta^{vac}}\right)\right]. \tag{13}$$

Moreover, as mentioned previously, composition analyses indicate that the oxygen stoichiometry is the same in all the as-deposited samples and in the annealed sample at 300 °C (temperature significantly lower than 700 °C). Therefore, the stress modifications cannot be attributed to a variation of the oxygen-vacancy concentration responsible for the nonstoichiometry. The stress changes are instead attributed to the change of AF defect concentrations. All the corresponding experimental straight lines [samples (1)–(5)] turn around the

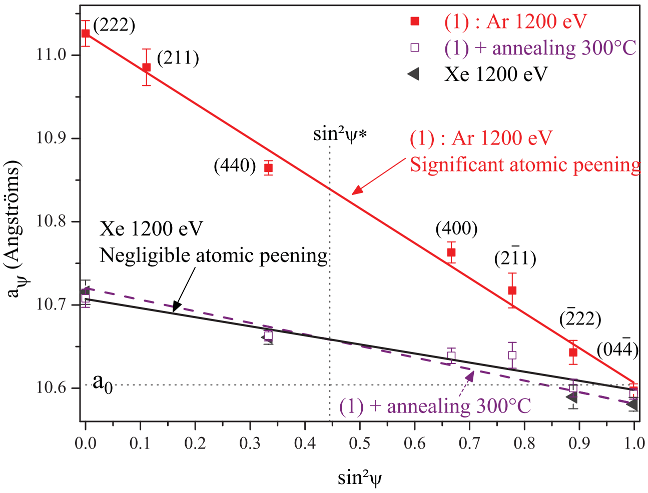

FIG. 13. (Color online) $a_\Psi = f(\sin^2\Psi)$ plots for as-deposited Y_2O_3 on Si using Ar and Xe ions at 1200 eV, before and after annealing at 300 °C in air.

same point and intersect at $\sin^2\Psi = 1$, which gives the characteristic value of $\beta^{\mathrm{AF}} = \beta_{\max} = 1.7$, from Eq. (12). In sample series (1)–(5), $\sigma_{\mathrm{hyd}}^{vac}$ is kept as constant and only $\sigma_{\mathrm{hyd}}^{\mathrm{AF}}$ is allowed to vary. The residual stress of the annealed sample at 300 °C [sample (5)] has been compared with an as-deposited thin film grown without atomic peening: indeed, if the primary Xe beam at 1200 eV is used (negligible number of backscattered ions), the experimental $a_\Psi = f(\sin^2\Psi)$ data coincide with the annealing at 300 °C (Fig. 13). Thus the sample annealed at 300 °C corresponds to the complete annihilation of the AF defects (i.e., $\sigma_{\mathrm{hyd}}^{\mathrm{AF}} = 0$). Consequently, the stress variations observed for the annealed sample from 300 °C to 1000 °C corresponding to the (5)–(9) series will be attributed to the single modification of the concentration of oxygen vacancies (i.e., modification of the fitting parameter $\sigma_{\mathrm{hyd}}^{vac}$ with $\sigma_{\mathrm{hyd}}^{\mathrm{AF}} = 0$). The intersection observed for $\sin^2\Psi \approx 0.7$ between the lines corresponds here to $\beta^{vac} = 0.8$.

Then, the experimental data were fitted simultaneously using Eq. (13) by adjusting $\sigma_{\mathrm{hyd}}^{vac}$ and $\sigma_{\mathrm{hyd}}^{\mathrm{AF}}$ respectively, in series (5)–(9) and (1)–(5) with the constraints mentioned just above, and keeping $a_0 = 10.604$ Å, $\beta^{vac} = 0.8$, and $\beta^{\mathrm{AF}} = 1.7$. The stress values deduced from the fits are reported in Table IV.

To improve the fits in the high $\sin^2\Psi$ values and to take into account an eventual variation of the in-plane stress (thermal, grain boundary [40,41]), an additional biaxial component of stress σ_{biax} was required, and the previous equation becomes

$$a_\Psi^{111} = a_0\left[1 + (s_{11} + 2s_{12})\left(\sigma_{\mathrm{hyd}}^{\mathrm{AF}} + \sigma_{\mathrm{hyd}}^{vac}\right)\right]\left[1 + \left(2s_{12} + \frac{2}{3}J + \frac{s_{44}}{2}\sin^2\Psi\right)\left(\sigma_{\mathrm{th}} + \sigma_{biax} - \frac{\sigma_{\mathrm{hyd}}^{\mathrm{AF}}}{\beta^{\mathrm{AF}}} - \frac{\sigma_{\mathrm{hyd}}^{vac}}{\beta^{vac}}\right)\right]. \tag{14}$$

The series of annealed samples (5)–(9) exhibits a decrease of the hydrostatic stress component $\sigma_{\mathrm{hyd}}^{vac}$, ascribed to the variation of vacancy defect concentrations, from 2.3 to 0.3 GPa (respectively for the 300 and 1000 °C annealing), with the fixed hydrostatic component $\sigma_{\mathrm{hyd}}^{vac}$ for all. For the (1)–(5) series, a strong increase of the hydrostatic stress component due to the AF defect variations is evidenced from 2.0 to 7.6 GPa (respectively for the as-deposited thin films grown in the energy ranges of 600 and 1200 eV), while the hydrostatic stress related to oxygen vacancies is constant ($\sigma_{\mathrm{hyd}}^{vac} = 2.3$ GPa).

V. DISCUSSION

A. Origin of the stress

The structural investigations coupled with stress analysis clearly point out the influence of the point defects on the residual stress in Y_2O_3 thin films deposited by means of IBS. The oxygen nonstoichiometry and the disorder on the constitutional oxygen-vacancy network (AF pairs) modify significantly the triaxial stress state in the films. The origin of these defects is attributed to the bombardment of the growing film by the backscattered particles (essentially coming from the Ar primary beam) from the target, which can acquire rather high energies (several hundred electron volts) depending on the primary energy. The average energies of these backscattered particles are found to change significantly from 54 to 108 eV (using the TRIM code [42] by reproducing the growth conditions from 600 to 1200 eV). These energies largely exceed the atomic displacement energies of Y and O atoms (around 25 eV). Therefore, a preferential resputtering of oxygen atoms at the surface of the growing film due to this atomic

TABLE IV. Stress state of Y_2O_3 thin films determined from the enhanced triaxial model. The stored elastic energy $w(\sigma)$ calculated by $w(\sigma) = \frac{1}{2}s_{ij}\sigma_i\sigma_j$ is also reported for as-deposited thin films.

	Triaxial model (Y_2O_3/Si) with $a_0 = 10.604$ Å and $\beta^{vac} = 0.8$ and $\beta^{\mathrm{AF}} = 1.7$									
Sample	$\sigma_{\mathrm{hyd}}^{\mathrm{eff}}$ (GPa)	$\sigma_{\mathrm{hyd}}^{\mathrm{AF}}$ (GPa)	$\sigma_{\mathrm{hyd}}^{vac}$ (GPa)	$\sigma_{\mathrm{fix}}^{\mathrm{eff}}$ (GPa)	$\sigma_{\mathrm{fix}}^{\mathrm{AF}}$ (GPa)	$\sigma_{\mathrm{fix}}^{vac}$ (GPa)	σ_{th} (GPa)	σ_{biax} (GPa)	Total biaxial stress (GPa)	$w(\sigma)$ (kJ/mol)
(1)	9.9 ± 1.3	7.6	2.3	−7.4 ± 0.9	−4.5	−2.9	0.6	1.0	−5.8	33.2
(2)	7.9 ± 1.1	5.6	2.3	−6.1 ± 0.9	−3.2	−2.9	0.6	0.7	−4.8	21.7
(3)	5.5 ± 0.6	3.2	2.3	−4.8 ± 0.6	−1.9	−2.9	0.6	0.4	−3.8	11.7
(4)	4.3 ± 0.9	2.0	2.3	−4.1 ± 0.8	−1.2	−2.9	0.6	0.4	−3.1	7.4
(5)	2.3 ± 0.6	0.0	2.3	−2.9 ± 0.8	0.0	−2.9	0.6	0.8	−1.5	
(6)	1.2 ± 0.6	0.0	1.2	−1.5 ± 0.8	0.0	−1.5	0.6	0.7	−0.2	
(7)	0.7 ± 0.3	0.0	0.7	−0.9 ± 0.4	0.0	−0.9	0.6	1.0	0.7	
(8)	0.3 ± 0.1	0.0	0.3	−0.4 ± 0.2	0.0	−0.4	0.6	0.7	0.9	

peening effect could be an explanation of the nonstoichiometry measured by RBS. Furthermore, these energetic particles can lead to the creation of AF pairs (oxygen-vacancy + interstitial), which exhibit one of the lowest formation energies of the possible point defects in this oxide. In oxides, point defects may be charged and have therefore a high ability to distort the atomic network and to modify the bond lengths due to electrostatic effects (such as ZnO[43] or $SrTiO_3$[44]). Extended defects can also induce strong strain fields whose symmetry and amplitude closely depend on their nature.[45] In cubic-*C* Y_2O_3, the consequence of removing an oxygen atom from one (48e) site is that the nearest yttrium atoms move slightly away from the vacancy site (because they are no longer attracted to it), and oxygen atoms move closer to the vacancy site as the charge repulsion effect decreases. For the oxygen interstitial in the (16c) site, the neighboring yttrium atoms move closer to the interstitial (electrostatic attraction), and the neighboring oxygen atoms move away from the interstitial (electrostatic repulsion).[16] Due to the thin-film geometry, the strain in this defective structure cannot be fully relaxed. Thus it is conceivable that the internal stress in Y_2O_3 thin films could be the direct consequence of the local distortions coming from the charged defects induced by atomic peening during the growth.

B. Results from the triaxial stress model

The use of the extended triaxial stress model enables to fit properly the experimental $a_\Psi = f(\sin^2\Psi)$ data, obtained from x-ray measurements, for the different appropriate samples and allows us to ascribe a physical meaning of the experimental variations (slope and intersection modifications). This modeling of the macroscopic residual stress in yttrium oxide thin films, based on nanometer-scale inclusions (point and extended defects) inducing an hydrostatic stress field in the matrix, leads to a possible quantitative analysis of the nature (large or small misfit) and of the concentration of the crystal defects inside the layer.

As mentioned previously, an additional biaxial component ($\sigma_{\rm biax}$) was required to improve the fits. However, this value is not predominant in the total stress and does not change significantly whatever the sample is (between 0.4 and 1.0 GPa). The β parameter found for AF defects ($\beta^{\rm AF} = 1.7$) is equal to the maximum value allowed by the model and corresponds to defects having a small misfit (i.e., defects of atomic size). For oxygen vacancies, $\beta^{vac} = 0.8$ is close to the minimum value allowed ($\beta_{\rm min} = 2/3$) and tends to show that these defects can be assimilated to a large misfit (i.e., defects larger than atomic size). The two values of β obtained from the experimental data are very close to the limit cases of large- and small-misfit particles (respectively 2/3 and 1.7). This result corroborates the nonmodification of the mechanical characteristics of the cubic-*C* structure (stiffness tensor, Young modulus) due to atomic or nanoscale inclusions. Thus, whatever the defect concentration, it appears possible to define the residual stress of the Y_2O_3 thin films as defined in Sec. IV B 1 (i.e., assuming that elastic constants between the matrix and the particles are the same). The large-misfit character obtained for vacancy defects appears as an essential result in the annealed samples between 300 and 1000 °C, where only the oxygen stoichiometry is allowed to change (AF concentration is zero and Ar concentration is constant), and it contributes to a better understanding of the particular arrangement of the excess of oxygen vacancies evidenced with the RBS analysis and the NRA. Considering the TEM experiments of the as-deposited films on $SrTiO_3$ and MgO substrates, which contains only one type of such an extended defect in the $\{111\}$ planes, the assignment of these defects to vacancy complex (or vacancy loops, clearly bigger than atomic size) seems to be coherent to match the large misfit character of defects identified with the extended triaxial stress modeling. Moreover this kind of vacancy arrangement is a well-known phenomenon which is typically observed in the strongly ionic oxides to accommodate an excess of oxygen vacancies. Such vacancy loops are expected to generate a quasi-spherical stress field (as for CeO_2 [46] or ZrO_2 [47]), in agreement with the hypothesis used in the triaxial formalism.

C. Stabilization of a new cubic phase after deposition?

Assuming a spherical symmetry, an average volume change induced by each type of point defect ($V_{\rm mis}$) can be estimated from the average distance between the nearest neighbor atoms for bulk and defect site in Y_2O_3 (from Ref. 16). For a single oxygen vacancy [on a (48e) site] and a single oxygen interstitial [on a (16c) site], the values $V_{\rm mis} = 2.890$ Å^3 and $V_{\rm mis} = 1.697$ Å^3 are obtained, respectively. Assuming that the volume change due to one AF is $V_{\rm mis}^{\rm AF} = V_{\rm mis}^{\rm vacancy} + V_{\rm mis}^{\rm interstitial}$ and using Eq. (5), the concentration of AF pair defects can be deduced from the hydrostatic stress component $\sigma_{\rm hyd}^{\rm AF}$. In the as-deposited thin films, the concentration of AF defects increases significantly with the primary energy. It is found to be about 3, 6, 10, and 13 AF/unit cell respectively for the deposition with an Ar beam at 600, 800, 1000, and 1200 eV. The two last values (10 and 13 AF/unit cell) may be sufficient to break the ordered constitutional oxygen-vacancy pattern [in the [16c) position] and thus to increase the symmetry of the structure from ($Ia\bar{3}$) to ($Fm\bar{3}m$). Consequently, the highly defective *C*-type structure of Y_2O_3 after a highly energetic deposition could be seen as a fluorite-like structure ($Fm\bar{3}m$) in which each cation is surrounded by eight anionic sites with 25% of oxygen vacancies per site. The results described above can thus be interpreted in terms of two different cubic structures which coexist in the as-deposited films. These two phases are in good agreement with the two different contrasts observed from HRTEM images [sample (9), Fig. 5] and with the asymmetric profile of the diffraction peak which can be seen as the sum of two cubic components [samples (1) and (2)]. Nevertheless, some unanswered questions can be broached such as the absence of the cubic-to-monoclinic transition observed usually in this strongly nonstoichiometric oxide. This seems to be due to a strong limiting oxygen-vacancy diffusion process during IBS thin-film growth (the monoclinic nucleus, i.e., the oxygen-vacancy loops, are not able to grow) compared with the AF rate creation by atomic peening.

This fluorite-like phase (also called X-type) was previously observed by Katagiri *et al.*[48] and Swamy *et al.*[2] in high-temperature conditions (> 2250 °C). However, it is still unclear whether this cubic disordered structure is a stable or metastable phase. Interestingly, the presence of such an unexpected disordered fluorite-derived structure was reported in Gd_2O_3 thin films after bombardment with Ne ions (1 keV).[49] Its stabilization was ascribed to the GaAs substrate that acts as a chemical and structural (epitaxy) template. The authors also mention a possible composition change, by the loss of O, to explain these observations. Since Gd only exists in the (3+) state, this hypothesis was rejected. However, as for yttrium oxide, where Y also only exists in the (3+) state, we strongly expect that a strong nonstoichiometry, accommodated by the formation of vacancy loops, the AF defects, and their related stress, acts as the main factor of stabilization of the fluorite-like phase (no influence of the substrate).

From these results arises a new question: Why does this X-type phase remain stable after IBS deposition performed at a much lower temperature (700 °C) and in particular after a deposition at high energy (Ar 1200 eV)? An answer can be proposed from a thermodynamical point of view by considering that the stored elastic energy (mostly due to the AF defects and the oxygen nonstoichiometry) could modify the stability of the C-type phase. The total stored elastic energy density $w(\sigma)$ can be easily calculated from our stress measurements, by $w(\sigma) = \frac{1}{2}s_{ij}\sigma_i\sigma_j$ (see Ref. 45), where s_{ij} are the components of the compliance tensor and σ_i and σ_j are the components of the stress tensor (in matrix notation).

Recently, the thermodynamical parameters in yttrium oxide were determined by Zinkevich[50] and Djurovic *et al.*[51] They expressed the Gibbs energies of the C phase (G^C) and the X phase (G^X) as functions of the temperature, T, using International System units (joule, mole, Kelvin). These quantities mainly differ from the entropy term due to the anionic disorder. Taking into account the stored elastic energy $w(\sigma)$ in the cubic-C structure (which is a stress-dependent function), the Gibbs energy of the defective C-type structure (labeled Cdef) is then modified and can be written, from Refs. 52 and 53, as

$$G^{\text{Cdef}}_{Y_2O_3}(T,\sigma) = G^{\text{C}}_{Y_2O_3}(T,0) + w(\sigma) \qquad (15)$$

Consequently, assuming a stress-free X phase, an increase of the stored elastic energy will modify the stability conditions of the defective C-type structure compared with the X type. The evolution of the variation of the Gibbs energy between these two phases is given as a function of T by

$$\begin{aligned}\Delta G^{\text{Cdef-X}}_{Y_2O_3}(T,\sigma) &= G^{\text{Cdef}}_{Y_2O_3}(T,\sigma) - G^{\text{X}}_{Y_2O_3}(T,0)\\ &= w(\sigma) - 37765 + 14.223T \qquad (16)\end{aligned}$$

On Fig. 14 are plotted the $\Delta G^{\text{Cdef-X}}_{Y_2O_3}(T,\sigma)$ evolutions as functions of T for the different values of the stored energy $w(\sigma)$ determined in Table IV. The positive (negative, respectively) values of $\Delta G^{\text{Cdef-X}}$ indicate that the X-type structure is more (less) stable than the defective C-type structure. These plots illustrate very well the influence of the stored elastic energy on the stabilization temperature of the X-type phase. Indeed for the bulk material [with $w(\sigma) = 0$], the domain of stability of the fluorite-like structure occurs for temperatures above 2350 °C, which is in good agreement with previous experimental observations.[2,48] For samples (4) and (3), the increase of the stored elastic energy lowered the temperature of stability of the X phase from 2350°C to approximately 1900°C and 1600°C, respectively. Sample (2) is very interesting because the calculation of $\Delta G^{\text{Cdef-X}}_{Y_2O_3}(T,\sigma)$ indicates that the critical temperature for the X-phase stabilization is closer to 700 °C, which corresponds to the deposition temperature. Now, if we consider sample (1) [deposition at the highest energy, corresponding to the highest stored elastic energy $w(\sigma) = 33.2$ kJ/mol], the domain of stability of the X-type structure extends toward the lower temperatures: in the growth conditions ($T=$ 700 °C), $\Delta G^{\text{Cdef-X}}_{Y_2O_3}(T,\sigma)$ is clearly positive, which indicates that the fluorite-like structure becomes the most stable structure.

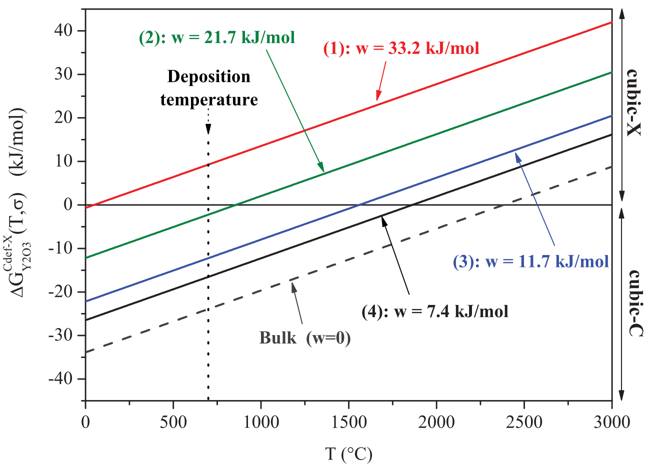

FIG. 14. (Color online) Evolution of $\Delta G^{\text{Cdef-X}}_{Y_2O_3}(T,\sigma)$ versus T, for different values of $w(\sigma)$.

VI. CONCLUSION

The present paper points out the influence of energetic growth of Y_2O_3 thin film by IBS on the formation of various crystal defects (AF pairs and oxygen-vacancy loops). It is evidenced that these defects are mainly due to the backscattered ions that knock on the film during the growth (“atomic peening effect”). The approach used in this paper shows the possibility of defining the X phase of Y_2O_3 like a highly defective cubic-C structure where both defects, AF and vacancy loops, act as key parameters to increase the symmetry of the cubic-C phase and to stabilize the metastable fluorite structure due to the stored energy induced by atomic and nanoscale defects. This method, based mainly on multiscale description of the residual stress, from the atomic size defects to the macroscopic measurement, demonstrates the importance and the correlation between the stability of particular defects and the stored elastic energy in the phase stabilization mechanisms under nonequilibrium process. This paper focused on samples elaborated by the IBS deposition technique, but it could enhance the field of modeling and understanding of other different non thermodynamic processes such as irradiation-induced phase transformations in fluorite-related compounds.[54–56]

ACKNOWLEDGMENT

The authors would like to acknowledge Dr. Philippe Guérin for helpful discussions and technical support with thin film depositions, and Dr. Jacques Perrière (Institut des Nanosciences de Paris) for RBS and NRA experiments.

[*] Current address: CIMAP, 6 Boulevard Maréchal Juin, 14050 Caen cedex 4, France.

[1] G. Adachi and N. Imanaka, Chem. Rev. **98**, 1479 (1998).

[2] V. Swamy, N. A. Dubrovinskaya, and L. S. Dubrovinsky, J. Mater. Res. **14**, 456 (1999).

[3] M. M. Kenisarin and V. Ya Chekhovskoy, Rev. Int. Hautes Temp. Refract. **12**, 329 (1975).

[4] Y. Guyot, R. Moncorgé, L. D. Merkle, A. Pinto, B. McIntosh, and H. Verdun, Opt. Mater. **5**, 127 (1996).

[5] M.-H. Cho, D.-H. Ko, Y. K. Choi, I. W. Lyo, K. Jeong, T. G. Kim, J. H. Song, and C. N. Whang, J. Appl. Phys. **89**, 1647 (2001).

[6] F. Jollet, C. Noguera, N. Thromat, M. Gautier, and J. P. Duraud, Phys. Rev. B **42**, 7587 (1990).

[7] J. Hao, S. A. Studenikin, and M. Cocivera, J. Lumin. **93**, 313 (2001).

[8] D. Dosev, B. Guo, and I. M. Kennedy, J. Aerosol Sci. **37**, 402 (2006).

[9] J. Kwo, M. Hong, A. R. Kortan, K. T. Queeney, Y. J. Chabal, J. P. Mannaerts, T. Boone, J. J. Krajewski, A. M. Sergent, and J. M. Rosamilia, Appl. Phys. Lett. **77**, 130 (2000).

[10] G. D. Wilk, R. M. Wallace, and J. M. Anthony, J. Appl. Phys. **89**, 5243 (2001).

[11] A. Dimoulas, A. Travlos, G. Vellianitis, N. Boukos, and K. Argyropoulos, J. Appl. Phys. **90**, 4224 (2001).

[12] J. Kwo, M. Hong, B. Busch, D. A. Muller, Y. J. Chabal, A. R. Kortan, J. P. Mannaerts, B. Yang, P. Ye, H. Gossmann, A. M. Sergent, K. K. Ng, J. Bude, W. H. Schulte, E. Garfunkel, and T. Gustafsson, J. Cryst. Growth **251**, 645 (2003); Proceedings of the Twelfth International Conference on Molecular Beam Epitaxy (Elsevier B.V., 2002), pp. 645-650.

[13] L. Marsella and V. Fiorentini, Phys. Rev. B **69**, 172103 (2004).

[14] F. D'Heurle and J. Harper, Thin Solid Films **171**, 81 (1989).

[15] F. Jollet, C. Noguera, M. Gautier, N. Thromat, and J.-P. Duraud, J. Am. Ceram. Soc. **74**, 358 (1991).

[16] J. X. Zheng, G. Ceder, T. Maxisch, W. K. Chim, and W. K. Choi, Phys. Rev. B **73**, 104101 (2006).

[17] S. H. N. Lim, D. G. McCulloch, M. M. M. Bilek, and D. R. McKenzie, J. Appl. Phys. **93**, 4283 (2003).

[18] A. E. Romanov, T. J. Baker, S. Nakamura, J. S. Speck, and E. U. Group (ERATO/JST UCSB Group), J. Appl. Phys. **100**, 023522 (2006).

[19] R. Menon, K. Sreenivas, and V. Gupta, J. Appl. Phys. **103**, 094903 (2008).

[20] A. R. Kaul, O. Y. Gorbenko, I. E. Graboy, S. V. Samoilenkov, M. A. Novojilov, A. A. Bosak, H. W. Zandbergen, and G. Wahl, Int. J. Inorg. Mater. **3**, 1177 (2001).

[21] R. J. Gaboriaud, F. Pailloux, P. Guerin, and F. Paumier, Thin Solid Films **400**, 106 (2001).

[22] C. Kisielowski, J. Krüger, S. Ruvimov, T. Suski, J. W. Ager, E. Jones, Z. Liliental-Weber, M. Rubin, E. R. Weber, M. D. Bremser, and R. F. Davis, Phys. Rev. B **54**, 17745 (1996).

[23] I. C. Noyan and J. B. Cohen, *Residual Stress: Measurement by Diffraction and Interpretation* (Springer, New York, 1987).

[24] L. R. Doolittle, Nucl. Instrum. Meth. Phys. Res. B **9**, 344 (1985).

[25] M. Mayer, SIMNRA user's guide (1997) [http://home.rzg.mpg.de/∼mam/index.html].

[26] F. Paumier and R. J. Gaboriaud, Thin Solid Films **441**, 307 (2003).

[27] R. J. Gaboriaud, F. Paumier, F. Pailloux, and P. Guerin, Mater. Sci. Eng. B **109**, 34 (2004), EMRS 2003, Symposium I, Functional Metal Oxides - Semiconductor Structures.

[28] R. J. Gaboriaud, F. Pailloux, and F. Paumier, Appl. Surf. Sci. **188**, 29 (2002).

[29] A. E. Solov'eva, Neorgan. Mater. **21**, 808 (1985).

[30] P. A. Stadelmann, Ultramicroscopy **21**, 131 (1987).

[31] B. G. Hyde, Acta Crystallogr. Sec. A **27**, 617 (1971).

[32] V. Hauk, W. K. Krug, R. W. M. Oudelhoven, and L. Pintschovius, Z. Metallkd. **79**, 159 (1988).

[33] B. M. Clemens and J. A. Bain, MRS Bull. **17**, 46 (1992).

[34] J. W. Palko, W. M. Kriven, S. V. Sinogeikin, J. D. Bass, and A. Sayir, J. Appl. Phys. **89**, 7791 (2001).

[35] J. D. Kamminga, T. H. de Keijser, R. Delhez, and E. J. Mittemeijer, Thin Solid Films **317**, 169 (1998).

[36] J.-D. Kamminga, T. H. de Keijser, R. Delhez, and E. J. Mittemeijer, J. Appl. Phys. **88**, 6332 (2000).

[37] G. Abadias and Y. Y. Tse, J. Appl. Phys. **95**, 2414 (2004).

[38] J. Eshelby, Solid State Phys. **3**, 79 (1956).

[39] Y. Okada and Y. Tokumaru, J. Appl. Phys. **56**, 314 (1984).

[40] R. Hoffman, Thin Solid Films **34**, 185 (1976).

[41] E. Chason, B. W. Sheldon, L. B. Freund, J. A. Floro, and S. J. Hearne, Phys. Rev. Lett. **88**, 156103 (2002).

[42] J. F. Ziegler and J. P. Biersack, Computer code SRIM 2008 program package [http://www.srim.org/].

[43] S. B. Zhang, S.-H. Wei, and A. Zunger, Phys. Rev. B **63**, 075205 (2001).

[44] D. A. Freedman, D. Roundy, and T. A. Arias, Phys. Rev. B **80**, 064108 (2009).

[45] J. Hirth and J. Lothe, *Theory of Dislocations*, 2nd ed. (John Wiley and Sons, Inc., New York, 1982).

[46] K. Yasunaga, K. Yasuda, S. Matsumura, and T. Sonoda, Nucl. Instrum. Methods Phys. Res. B **266**, 2877 (2008), Proceedings of the Fourteenth International Conference on Radiation Effects in Insulators.

[47] A. Ryazanov, K. Yasuda, C. Kinoshita, and A. Klaptsov, J. Nucl. Mater. **307-311**, 918 (2002).

[48] S. Katagiri, N. Ishizawa, and F. Marumo, Powder Diffr. **8**, 60 (1993).

[49] C. Steiner, B. Bolliger, M. Erbudak, M. Hong, A. R. Kortan, J. Kwo, and J. P. Mannaerts, Phys. Rev. B **62**, R10614 (2000).

[50] M. Zinkevich, Prog. Mater. Sci. **52**, 597 (2007).

[51] D. Djurovic, M. Zinkevich, and F. Aldinger, Solid State Ionics **179**, 1902 (2008).

[52] D. Balzar, P. A. Ramakrishnan, and A. M. Hermann, Phys. Rev. B **70**, 092103 (2004).

[53] A. Gheribi, J. Rogez, and J. Mathieu, Calphad **32**, 315 (2008).

[54] J. Lian, L. M. Wang, S. X. Wang, J. Chen, L. A. Boatner, and R. C. Ewing, Phys. Rev. Lett. **87**, 145901 (2001).

[55] J. Lian, J. Chen, L. M. Wang, R. C. Ewing, J. M. Farmer, L. A. Boatner, and K. B. Helean, Phys. Rev. B **68**, 134107 (2003).

[56] M. Tang, P. Lu, J. A. Valdez, and K. E. Sickafus, J. Appl. Phys. **99**, 063514 (2006).